ЖЭТФ/JETP, 2026, том 170, вып. 6 (12), стр. 548–560 © 2026

ACCRETION DISK AROUND CHARGED BLACK HOLES WITH NONLINEAR ELECTRODYNAMICS

R. M. Yusupova [a,b*], ***R. Kh. Karimov*** [a], ***R. N. Izmailov*** [a]

[a] *Zel'dovich International Center for Astrophysics, M. Akmullah Bashkir State Pedagogical University 450077, Ufa, Russia*

[b] *Institute of Molecule and Crystal Physics, Ufa Federal Research Centre of the Russian Academy of Sciences 450075, Ufa, Russia*

Received May 4, 2026
revised version August 24, 2026
Accepted for publication September 23, 2026

We investigate a geometrically thin, optically thick accretion disk around a charged regular Balart – Vagenas black hole and compare its kinematic and radiative properties with those of the Reissner – Nordström, Schwarzschild, and tidal charged black holes. Restricting the parameter to $a = 1$, which provides the charge correction in the asymptotic expansion, we examine two values of the parameter γ, namely $\gamma = 1/2$ and $\gamma = 1/6$. We compute the horizon radius, the marginally stable orbit, the flux, the temperature distribution, the spectral luminosity, and the accretion efficiency for a stellar-mass compact object with $M = 15M_\odot$ and $\dot{M}_0 = 10^{19}$ g/s. For both values of γ, increasing the charge shifts the marginally stable orbit inward and increases the accretion efficiency. The influence of the parameter γ on the radiative properties of the disk is also demonstrated. At $\gamma = 1/2$, the Balart – Vagenas black hole yields substantially larger flux, temperature, and spectral maxima than in the Reissner – Nordström and Schwarzschild cases, whereas for $\gamma = 1/6$ it remains close (but not identical) to the Reissner – Nordström solution. For a more accurate analysis, we also normalize the metric charge by the asymptotic charge $Q_{\rm as}^2 = 6\gamma q^2$. For $a = 1$, the Balart – Vagenas metric and all thin accretion disk observables depend on γ and q only through $Q_{\rm as}$, and consequently the results for $\gamma = 1/6$ and $\gamma = 1/2$ coincide exactly at fixed $Q_{\rm as}/M$. At $Q_{\rm as}/M = 0.5$, the flux, temperature, and spectral maxima of the Balart – Vagenas black hole are lower than the corresponding Reissner – Nordström black hole values by approximately 0.61%, 0.15%, and 0.19%, respectively. Therefore, the large enhancement found at fixed q/M is primarily associated with the different charge normalization and proximity to extremality, whereas the residual nonlinear electrodynamic correction at fixed asymptotic charge is small. In the case of tidal charge, the accretion parameters of the charged black hole turn out to be lower than in the classical cases. Thus, depending on the parameters of nonlinear electrodynamics in the Balart – Vagenas solution, the accretion characteristics can either mimic the classical charged solution or lead to significantly more intense radiation.

Keywords: regular black holes, nonlinear electrodynamics, Balart – Vagenas metric, thin accretion disk, Novikov – Thorne model, accretion efficiency

DOI: 10.31857/S0044451026120033

1. INTRODUCTION

The issue of singularities remains one of the unresolved challenges in black hole physics. General relativity, despite its success, fails to provide a complete resolution to this problem. To advance our understanding of the physical universe, it becomes necessary either to eliminate singularities through alternative theories of gravity or to extend general relativity itself, for example, by coupling gravity to theories of nonlinear electrodynamics. This has led to the development of numerous models proposing the existence of charged regular black holes, in which the classical singularity is replaced by a region of finite density hidden behind the event horizon. Charged regular black holes are solutions of Einstein

* E-mail: yu.rose@mail.ru

equations that have horizons and, contrary to Reissner – Nordström black holes which have singularities at the origin, are regular everywhere [1].

In suitable astrophysical environments, compact objects such as black holes and neutron stars can be surrounded by accretion disks. In the context of the geometrically thin, optically thick Novikov – Thorne model, the disk matter is described as gas or plasma moving on nearly Keplerian circular orbits. This assumption does not apply to all accretion flows: thick disks, slim disks, ADAF/RIAF solutions, and magnetohydrodynamic flows can be non-Keplerian. Observations show that accretion disks have sizes from tens to hundreds of parsecs [2, 3]. Important studies in the Newtonian approximation are described in [4]. Later, a general relativistic model of a thin accretion disk was developed in three seminal papers by Novikov and Thorne [5], Page and Thorne [6, 7]. To date, there also exist many important works in the field of accretion phenomena (see, e.g., [8–14]). Moreover, the main goal of accretion disk theory is to better understand the nature of black holes themselves.

Thin accretion disks have also been widely used as probes of modified and alternative theories of gravity. For example, Novikov – Thorne disks around black holes in hybrid metric-Palatini gravity [15, 16], Hořava gravity [17], Chern – Simons modified gravity [18], $f(R)$ models [19, 20], and Einstein – scalar – Gauss – Bonnet gravity [21] show that changes in the underlying spacetime can shift the marginally stable orbit, modify the flux and temperature distributions, and change the emitted spectrum and accretion efficiency. Related relativistic MHD studies further demonstrate that magnetic fields and angular momentum transport can strongly affect accretion and jet formation [22]. These works show that disk observables provide a useful diagnostic of strong field gravity and motivate the comparison of regular nonlinear electrodynamic black holes with the standard Schwarzschild and Reissner – Nordström geometries.

In this work, we focus on a specific class of black holes, the Balart – Vagenas black hole (hereinafter BVBH) with electric charge [1]. We then compare their thin accretion disk profiles with the known profiles for the Schwarzschild black hole (SBH), Reissner – Nordström black hole (RNBH) [23], and tidal charged black hole (TCBH) [24]. These solutions reduce to the SBH solution when the electric charge vanishes. In [25], the phenomenon of gravitational lensing in the strong-field regime was studied for a regular, static, charged black hole with a source of nonlinear electrodynamics. The deflection angle was obtained and compared with those of the SBH and the RNBH, which possess similar properties.

The comparison between the BVBH and RNBH is physically motivated by the different electromagnetic theories from which they arise. The RNBH geometry is the standard charged black hole solution of Einstein gravity coupled to linear Maxwell electrodynamics. It contains a curvature singularity at the origin. By contrast, the BVBH geometry is obtained by coupling general relativity to nonlinear electrodynamics, in which the electromagnetic source is described by a nonlinear Lagrangian $L(F)$. This nonlinear behavior becomes relevant mainly in the strong field region and can remove the central singularity while preserving the appropriate weak field behavior. Therefore, comparing these two solutions allows one to separate the effects of electric charge itself from the effects caused by nonlinear electromagnetic corrections.

Earlier studies of disk accretion onto regular charged black holes were published, for example, in [9], where the influence of free parameters in the Dymnikova and Fan – Wang solutions on disk characteristics was investigated. Using the Einstein and Møller energy-momentum complexes, the distribution of energy and momentum for a spherically symmetric charged nonsingular black hole was investigated in [26]. In [27], the equivalence between the BVBH and the RNBH was studied. The main conclusion is that these two black holes are equivalent in terms of orbital dynamics outside the event horizons, which allows, in some cases, replacing the RNBH with a regular nonsingular black hole. Tidal effects around regular black holes were studied in [28]. By numerically solving the equations, it was found that under the action of tidal forces, a particle may undergo compression or stretching in the radial and angular directions.

The novelty of the present work lies in applying the Novikov – Thorne model to the regular charged BVBH and directly comparing its disk observables with those of the SBH, RNBH, and TCBH under the same disk parameters. We focus on $a = 1$ because this case contains the leading RNBH-type charge correction in the asymptotic expansion. The two values $\gamma = 1/6$ and $\gamma = 1/2$ are first considered at fixed values of the original parameter q/M in order to illustrate the behavior of the corresponding parameter sequences. We subsequently introduce the asymptotically normalized metric charge $Q_{\rm as}^2 = 6\gamma q^2$ and perform a controlled comparison at fixed $Q_{\rm as}/M$. This comparison reveals an exact (γ, q) degeneracy for all neutral particle metric-based observables when $a = 1$: only the combination $Q_{\rm as}$, rather than γ and q separately, can be constrained through

the Novikov – Thorne disk model considered here.

It should be noted that in realistic astrophysical environments, the electric charge of a black hole is expected to be quickly neutralized by the surrounding plasma. Therefore, in the present study, q should be considered as a parameter of the regular nonlinear electrodynamic solution and as a probe of possible strong field deviations from the SBH and RNBH geometries.

The paper is organized as follows. We briefly summarize the main characteristics of the charged regular black hole solution in Sec. 2. In Sec. 3, we study the circular geodesics and the marginally stable orbit. In Sec. 4, assuming a toy model of this black hole, we compute the emissivity profiles and compare them with those of the RNBH, SBH, and TCBH. In Sec. 5, we introduce the asymptotically normalized charge and perform comparisons at fixed charge. We discuss and conclude our results in Sec. 6. We use units such that $8\pi G = c = 1$ and the metric signature $(-,+,+,+)$.

2. BALART – VAGENAS SOLUTIONS

L. Balart and E. C. Vagenas constructed several charged regular black hole metrics [1] within the framework of general relativity coupled to nonlinear electrodynamics through a term $L(F)$ in the action, where $F = \frac{1}{4}F^{\mu\nu}F_{\mu\nu}$ is the Lorentz-invariant scalar and $F^{\mu\nu}$ is the electromagnetic field tensor, which reduces to the standard Maxwell tensor in the weak field limit. The new metric function has been obtained using the Dagum distribution [1, 29], which makes it possible to obtain a metric regular everywhere and satisfying the weak energy condition (WEC),

$$\sigma(r) = \left\{1 + \left(\frac{q^2}{Mr}\right)^a\right\}^{-(1+1/a)}, \qquad (1)$$

where $\sigma(r)$ is the distribution function, a is the dimensionless parameter, and M and q are the mass and the charge of the black hole, respectively. A distribution function $\sigma(r)$ is a normalized radial function, inspired by probability distributions, that controls how the black hole mass is spread with radius to avoid singularities.

We consider one of the solutions describing a new spherically symmetric, static, charged nonsingular black hole that satisfies the WEC. The corresponding metric has a line element of the form

$$ds^2 = -f(r)\,dt^2 + f^{-1}(r)\,dr^2 + r^2(d\theta^2 + \sin^2\theta\,d\phi^2), \qquad (2)$$

$$f(r) = 1 - \frac{2M}{r}\left[\frac{1}{1+\gamma\left(\frac{q^2}{Mr}\right)^a}\right]^{3/a}, \qquad (3)$$

where the parameter γ controls the strength of the nonlinear electrodynamic correction, while the parameter a determines how this correction enters the asymptotic expansion.

The expression of the corresponding electric field is of the form [1]

$$E = \frac{q}{r^2}\,\frac{3\gamma(3+a)}{2}\left(\frac{q^2}{Mr}\right)^{a-1} \times \left\{1+\gamma\left(\frac{q^2}{Mr}\right)^a\right\}^{-(2a+3)/a}. \qquad (4)$$

Next, we expand $f(r)$ in powers of M/r for different values of a. So we have, for $a = 1$,

$$f(r) = 1 - \frac{2M}{r} + 6\gamma\left(\frac{q}{M}\right)^2\left(\frac{M}{r}\right)^2 - 12\gamma^2\left(\frac{q}{M}\right)^4\left(\frac{M}{r}\right)^3 + 20\gamma^3\left(\frac{q}{M}\right)^6\left(\frac{M}{r}\right)^4 - 30\gamma^4\left(\frac{q}{M}\right)^8\left(\frac{M}{r}\right)^5 + \ldots = 1 + \sum_{n=1}^{\infty}(-1)^n(n^2+n)\,\gamma^{n-1} \times \left(\frac{q}{M}\right)^{2(n-1)}\left(\frac{M}{r}\right)^n, \qquad (5)$$

for $a = 2$,

$$f(r) = 1 - \frac{2M}{r} + 3\gamma\left(\frac{q}{M}\right)^4\left(\frac{M}{r}\right)^3 - \frac{15\gamma^2}{4}\left(\frac{q}{M}\right)^8\left(\frac{M}{r}\right)^5 + \ldots = 1 + \sum_{n=1}^{\infty}\frac{(-1)^n}{2^{2n-2}}\,\frac{(2n)!}{n!(n-1)!}\,\gamma^{n-1} \times \left(\frac{q}{M}\right)^{4(n-1)}\left(\frac{M}{r}\right)^{2n-1}, \qquad (6)$$

and for $a = 3$,

$$f(r) = 1 - \frac{2M}{r} + 2\gamma\left(\frac{q}{M}\right)^6\left(\frac{M}{r}\right)^4 + \ldots = 1 + \sum_{n=1}^{\infty}2(-1)^n\gamma^{n-1}\left(\frac{q}{M}\right)^{6(n-1)}\left(\frac{M}{r}\right)^{3n-2}. \qquad (7)$$

For $a = 1$, the expansion contains a charge-dependent term proportional to q^2/r^2, which makes this case directly comparable with the RNBH weak field expansion. For $a = 2$ and $a = 3$, the leading charge-dependent corrections appear at higher orders, namely at order $(M/r)^3$ and $(M/r)^4$, respectively. Therefore, in the present work we restrict ourselves to $a = 1$, for which the comparison with the RN-type charge correction is most transparent. Then, the BVBH metric (2), (3) reduces to

$$ds^2 = -f(r)\,dt^2 + f^{-1}(r)\,dr^2 + \\ + r^2(d\theta^2 + \sin^2\theta\,d\phi^2), \quad (8)$$

$$f(r) = 1 - \frac{2M}{r}\left(1 + \frac{\gamma q^2}{Mr}\right)^{-3}. \quad (9)$$

The black hole solution (8), (9) reduces to the SBH solution for $q = 0$. For $a = 1$ and $\gamma = 1/6$, the metric reproduces the RNBH asymptotic form up to the leading charge-dependent term, while higher order nonlinear electrodynamic corrections remain. Therefore, the $\gamma = 1/6$ BVBH geometry is RNBH-like in the weak field leading charge term, but it is not exactly identical to the RNBH spacetime. Except for particular choices of a and γ, the nonsingular black hole geometries associated with the metric function (3) do not asymptotically approach the RNBH solution. It is important to note that the TCBH metric can be obtained from the RNBH metric using the complex charge transformation $q \to iq$. A solution for a black hole with a tidal charge was obtained by Dadhich, Maartens, Papadopoulos, and Rezania [24]; it describes a regime of strong gravity on the brane (see also [30]). They found that the solution of the effective Einstein equations on the brane resembles the RNBH solution without the usual electric charge, but instead with a tidal charge as a five-dimensional imprint on the brane [31].

Given $f(r)$, the extremal case, where the equation $f(r) = 0$ has only one root, is defined by the conditions

$$f(r) = 0, \quad \frac{df}{dr} = 0. \quad (10)$$

Using conditions (10), we can find the critical charge q_c, which is given by

$$\frac{q_c}{M} = \sqrt{\frac{8}{27\gamma}}. \quad (11)$$

Note that for $q < q_c$, the metric function $f(r)$ has two positive roots, $r_{\mathrm{h}-}$ and $r_{\mathrm{h}+}$, which are obtained numerically from the equation $f(r_{\mathrm{h}}) = 0$. At $q = q_c$, the two horizons coincide, while for $q > q_c$ no event horizon exists.

Table 1. Critical value of charge q_c for which $f(r) = 0$ has only one root

γ	q_c
1/2	$0.76980\,M$
1/6	$1.33333\,M$

For clarity, the values of the critical charges are shown in Table 1. For $\gamma = 1/2$, the critical charge is $q_c \approx 0.7698M$, so the largest tabulated value $q = 0.769M$ is essentially extremal, whereas for $\gamma = 1/6$, $q_c \approx 1.333M$, so even $q = M$ reaches only about 75% of the critical limit. One can assume that the $\gamma = 1/2$ case exhibits much more significant strong field behavior because it is considered almost exactly in the extremal configuration, while the $\gamma = 1/6$ case is still comparatively far from its own limiting case.

3. KINEMATIC PROPERTIES OF THE THIN ACCRETION DISK

We use the standard relativistic thin accretion disk model developed by Novikov and Thorne for stationary, axisymmetric spacetimes. This framework adopts the equatorial approximation and is built on several key assumptions.

The disk is geometrically thin ($h \ll r$) and optically thick ($l \ll h$). The disk is in hydrodynamical and thermodynamic equilibrium, radiates as a black body, and efficiently converts all gravitational energy into heat and electromagnetic radiation. The disk lies in the equatorial plane, with its inner edge defined by the marginally stable (ms) orbit r_{ms}, or innermost stable circular orbit (ISCO), and its outer boundary at r_{out}. The particles in the disk follow nearly geodesic, circular orbits, with their trajectories dictated entirely by the underlying spacetime geometry.

Integration of the geodesic equation yields the effective potential $V_{\mathrm{eff}}(r)$, which for metric (8), (9) is given by

$$V_{\mathrm{eff}}(r) = \left\{1 - \frac{2M}{r}\left(1 + \frac{\gamma q^2}{Mr}\right)^{-3}\right\}\left(1 + \frac{\widetilde{L}^2}{r^2}\right). \quad (12)$$

The existence of circular orbits at any arbitrary radius r in the equatorial plane demands that $V_{\mathrm{eff}}(r) = \widetilde{E}^2(r)$ and $dV_{\mathrm{eff}}(r)/dr = 0$. These conditions allow us to calculate the angular velocity $\Omega(r)$, the specific energy

Table 2. The radii r_{h+} and r_{ms} for the BVBH for different values of γ and q compared with the RNBH and TCBH

BVBH					
$\gamma = 1/2$			$\gamma = 1/6$		
q/M	r_{h+}/M	r_{ms}/M	q/M	r_{h+}/M	r_{ms}/M
0	2.0000	6.0000	0	2.0000	6.0000
0.25	1.9047	5.7155	0.25	1.9886	5.9059
0.5	1.5948	4.8124	0.5	1.8722	5.6191
0.75	0.8438	2.9296	0.75	1.7030	5.1233
0.769	0.6402	2.6846	1	1.4399	4.3768
RNBH			TCBH		
q/M	r_{h+}/M	r_{ms}/M	q/M	r_{h+}/M	r_{ms}/M
0	2.0000	6.0000	0	2.0000	6.0000
0.25	1.9682	5.9052	0.25	2.0308	6.0927
0.5	1.8660	5.6066	0.5	2.1180	6.3600
0.75	1.6614	5.0465	0.75	2.2500	6.7748
1	1.0000	4.0000	1	2.4142	7.3067

$\widetilde{E}(r)$, and the specific angular momentum $\widetilde{L}(r)$ of particles moving in circular orbits in the above geometry:

$$\Omega(r) = \frac{M^2\sqrt{Mr - 2\gamma q^2}}{\left(Mr + \gamma q^2\right)^2}, \tag{13}$$

$$\widetilde{E}(r) = \frac{\left(Mr + \gamma q^2\right)^3 - 2M^4 r^2}{\left(Mr + \gamma q^2\right)\sqrt{\left(Mr + \gamma q^2\right)^4 - 3M^5 r^3}}, \tag{14}$$

$$\widetilde{L}(r) = \frac{M^2 r^2\sqrt{Mr - 2\gamma q^2}}{\sqrt{\left(Mr + \gamma q^2\right)^4 - 3M^5 r^3}}. \tag{15}$$

The stability of orbits depends on the sign of $d^2V_{\text{eff}}(r)/dr^2$, while the condition $d^2V_{\text{eff}}(r)/dr^2 = 0$ gives the marginally stable orbit at $r = r_{ms}$.

In the steady-state thin disk model, the quantities Ω, $\widetilde{E}$, and $\widetilde{L}$ of the orbiting particles depend only on the radii of the orbits.

Table 2 shows that the basic kinematic effect of charge is an inward shift of the outer horizon r_{h+} and, more importantly, an inward shift of the marginally stable orbit r_{ms} for both BVBH cases and for the RNBH case. For the BVBH with $\gamma = 1/2$, r_{ms} decreases from $6M$ at $q = 0$ to $2.6846M$ at $q = 0.769M$, a reduction of about 55.3%. For $\gamma = 1/6$, r_{ms} decreases to $4.3768M$ at $q = M$, i. e., by about 27.1%. By contrast, the TCBH behaves in the opposite way: both r_{h+} and r_{ms} move outward as the charge increases, which already suggests that its disks should become cooler and less radiatively efficient. A similar outward displacement of the marginally stable orbit in the TCBH geometry was reported by Alexeyev et al. [32], who analyzed the strong field properties of a phenomenological extension of the TCBH solution.

4. EMISSIVITY PROPERTIES

The emissivity properties include the energy flux emitted by the disk $F(r)$, the temperature distribution $T(r)$, the luminosity spectra $L(\nu)$, and the efficiency ε. Thorne [6], using the rest mass conservation law, showed that the time-averaged rate of rest mass accretion dM_0/dt is independent of the radius:

$$\dot{M}_0 \equiv dM_0/dt = -2\pi r u_r \Sigma = \text{const}.$$

Here, t and r are the coordinate time and radial coordinate, respectively, u_r is the radial component of the four-velocity u_μ of the accreting particles, and Σ is the averaged surface density of the disk.

The flux F of the radiant energy over the disk can be expressed in terms of Ω, $\widetilde{E}$, and $\widetilde{L}$ as

$$F(r) = -\frac{\dot{M}_0}{4\pi\sqrt{-g}}\,\frac{\Omega_{,r}}{(\widetilde{E} - \Omega\widetilde{L})^2} \times \\ \times \int_{r_{ms}}^{r} (\widetilde{E} - \Omega\widetilde{L})\widetilde{L}_{,r}\, dr. \tag{16}$$

Note that for the equatorial disk ($\theta = \pi/2$), the determinant of the metric tensor entering the Page – Thorne flux equation is

$$\sqrt{-g} = \sqrt{-g_{tt}g_{rr}g_{\phi\phi}} = r.$$

The expression $\sqrt{-g}$ contains the Jacobian arising from the transition to the radial coordinate in a static spherically symmetric metric. With this choice, the $q = 0$ limit for all considered spacetimes reproduces the normalization for the thin disk according to the Novikov – Thorne model in the SBH case. The radiation flux emitted by the disk surface follows the Stefan – Boltzmann law

$$F(r) = \sigma_{SB} T^4(r), \tag{17}$$

where σ_{SB} is the Stefan – Boltzmann constant. The observed luminosity $L(\nu)$ has a redshifted black body spectrum

$$L_\nu = 4\pi d^2 I(\nu) = \\ = \frac{8\pi h\cos i}{c^2}\int_{r_{in}}^{r_f}\int_{0}^{2\pi} \frac{\nu_e^3 r\, dr\, d\varphi}{\exp\left(h\nu_e/k_B T\right) - 1}, \tag{18}$$

where i is the disk inclination angle, d is the distance between the observer and the center of the disk, $r_{\rm in}$ and $r_{\rm f}$ are the inner and outer radii of the disk, h is the Planck constant, ν_e is the emission frequency, $I(\nu)$ is the Planck distribution, and $k_{\rm B}$ is the Boltzmann constant. The observed photons are redshifted, and their frequency ν is related to that of the emitted ones as $\nu_e = (1+z)\nu$. The redshift factor $(1+z)$ has the form [33–35]

$$1+z = \frac{1+\Omega r \sin\varphi \sin i}{\sqrt{-g_{tt} - \Omega^2 g_{\varphi\varphi}}}, \tag{19}$$

where the light bending effect is neglected.

The efficiency is measured at infinity and is defined as the ratio of two rates: the rate of energy of the photons emitted from the disk surface and the rate with which the mass-energy is transported to the central body. If all photons reach infinity, an estimate of the efficiency is given by the specific energy of the accreting particles measured at the marginally stable orbit:

$$\varepsilon = 1 - \widetilde{E}_{\rm ms}. \tag{20}$$

It is clear from Eq. (20) that the efficiency of accretion as an energy release mechanism is strongly dependent on the compactness of the accreting object: the larger the ratio M/r, the greater the efficiency. We use the above formulas to compute the emissivity properties numerically. We consider for illustration the central compact object of mass $M = 15M_\odot$ with an accretion rate $\dot{M}_0 = 10^{19}$ g/s. The inner boundary of the accretion disk is determined by the marginally stable radius $r_{\rm ms}$, which, for the BVBH solution, depends on the charge q, as presented in Table 2. As seen from Table 2, with the increase in $q \leqslant M$, the radii $r_{\rm ms}$ decrease for the BVBH, and the efficiency ε increases. In the case of the RNBH, with the increase in $q \leqslant M$, the radii $r_{\rm ms}$ decrease and the efficiency ε increases. The TCBH exhibits the opposite trend.

Table 3 demonstrates the effect of the metric parameters on the emissivity properties of the disk. For small values of the electric charge, the disk profiles for the black hole models under consideration are indistinguishable from those of the SBH. At $q = 0.25M$ and $\gamma = 1/6$, the BVBH and RNBH are almost indistinguishable in $F_{\max}$, $T_{\max}$, and $\nu L(\nu)_{\max}$. The strong difference occurs only at larger charge, especially for $\gamma = 1/2$. In that case, $F_{\max}$ rises from $2.4644 \cdot 10^{22}$ to $2.314 \cdot 10^{23}$ erg s^{-1} cm^{-2}, which is about 10 times higher than for the SBH and roughly 3.14 times the RNBH value at its peak. Also, for $\gamma = 1/2$, the maximum value of $F(r)$ increases by about 4 times as the charge increases from $q = 0.5M$ to $q = 0.75M$. In the case of the TCBH, as the charge increases, the values of $F_{\max}$, $T_{\max}$, and $\nu L(\nu)_{\max}$ decrease.

Table 3. The exact maximum values of the time-averaged radiation flux $F_{\max}$, temperature $T_{\max}$, and emission spectra $\nu L(\nu)_{\max}$ for the accretion disks around the BVBH for different values of γ and q compared with the RNBH and TCBH

q/M	$F_{\max}$, erg s^{-1} cm^{-2}	$T_{\max}$, K	$\nu L(\nu)_{\max}$, erg s^{-1}
BVBH			
$\gamma = 1/2$			
0	$2.4644 \cdot 10^{22}$	$4.5659 \cdot 10^{6}$	$4.8444 \cdot 10^{38}$
0.25	$2.8343 \cdot 10^{22}$	$4.7284 \cdot 10^{6}$	$5.0601 \cdot 10^{38}$
0.5	$4.6358 \cdot 10^{22}$	$5.3472 \cdot 10^{6}$	$5.8898 \cdot 10^{38}$
0.75	$1.8376 \cdot 10^{23}$	$7.5450 \cdot 10^{6}$	$8.8641 \cdot 10^{38}$
0.769	$2.3140 \cdot 10^{23}$	$7.9926 \cdot 10^{6}$	$9.4600 \cdot 10^{38}$
$\gamma = 1/6$			
0	$2.4644 \cdot 10^{22}$	$4.5659 \cdot 10^{6}$	$4.8444 \cdot 10^{38}$
0.25	$2.5630 \cdot 10^{22}$	$4.6182 \cdot 10^{6}$	$4.9137 \cdot 10^{38}$
0.5	$2.9763 \cdot 10^{22}$	$4.7868 \cdot 10^{6}$	$5.1375 \cdot 10^{38}$
0.75	$3.8780 \cdot 10^{22}$	$5.1139 \cdot 10^{6}$	$5.5757 \cdot 10^{38}$
1	$6.0665 \cdot 10^{22}$	$5.7192 \cdot 10^{6}$	$6.3927 \cdot 10^{38}$
RNBH			
0	$2.4644 \cdot 10^{22}$	$4.5659 \cdot 10^{6}$	$4.8444 \cdot 10^{38}$
0.25	$2.5801 \cdot 10^{22}$	$4.6186 \cdot 10^{6}$	$4.9142 \cdot 10^{38}$
0.5	$2.9947 \cdot 10^{22}$	$4.7939 \cdot 10^{6}$	$5.1471 \cdot 10^{38}$
0.75	$4.0411 \cdot 10^{22}$	$5.1668 \cdot 10^{6}$	$5.6444 \cdot 10^{38}$
1	$7.3645 \cdot 10^{22}$	$6.0032 \cdot 10^{6}$	$6.7594 \cdot 10^{38}$
TCBH			
0	$2.4644 \cdot 10^{22}$	$4.5659 \cdot 10^{6}$	$4.8444 \cdot 10^{38}$
0.25	$2.3494 \cdot 10^{22}$	$4.5157 \cdot 10^{6}$	$4.7779 \cdot 10^{38}$
0.5	$2.0827 \cdot 10^{22}$	$4.3777 \cdot 10^{6}$	$4.5959 \cdot 10^{38}$
0.75	$1.7340 \cdot 10^{22}$	$4.1817 \cdot 10^{6}$	$4.3383 \cdot 10^{38}$
1	$1.4045 \cdot 10^{22}$	$3.9672 \cdot 10^{6}$	$4.0466 \cdot 10^{38}$

Figure 1 reveals an important qualitative contrast among the four spacetimes. In the BVBH and RNBH cases, increasing charge shifts the flux peak inward and upward, meaning that the maximum of $F(r)$ shifts closer to the central object. In the TCBH case, the opposite happens: the peak moves outward and downward, and the overall profile weakens. This is exactly consistent with the outward shift of $r_{\rm ms}$ in Table 2. However, it should be noted that the four plots use different vertical scales, so the visual height of the curves

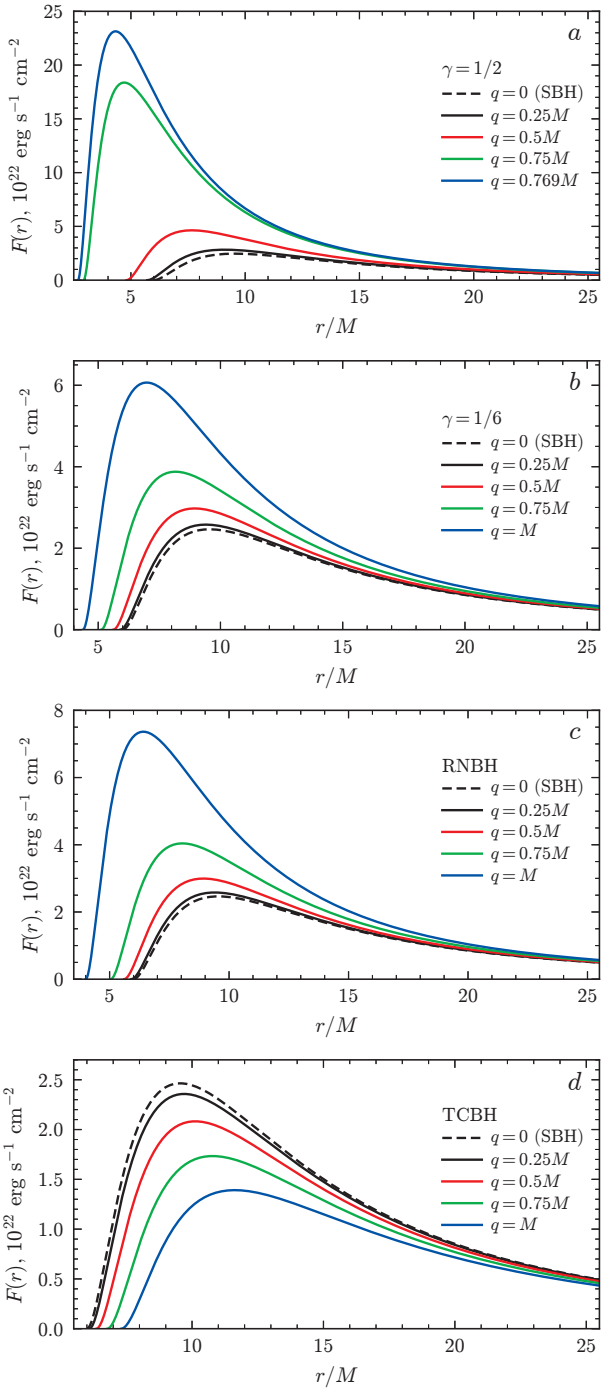


Fig. 1. Time-averaged radiation flux $F(r)$ for thin accretion disks around the BVBH with $\gamma = 1/2$ (*a*), the BVBH with $\gamma = 1/6$ (*b*), the RNBH (*c*), and the TCBH (*d*). For both BVBH cases, we set $a = 1$ and plot for different charges q/M

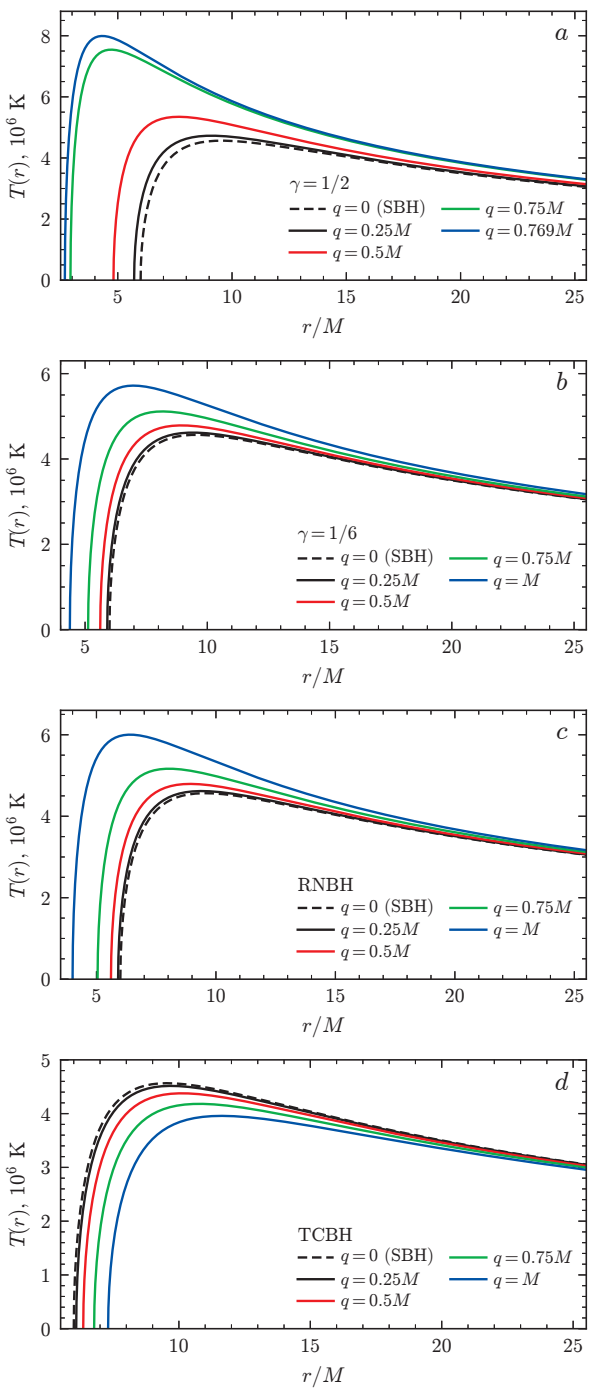


Fig. 2. Temperature distribution $T(r)$ for thin accretion disks around the BVBH with $\gamma = 1/2$ (*a*), the BVBH with $\gamma = 1/6$ (*b*), the RNBH (*c*), and the TCBH (*d*). For both BVBH cases, we set $a = 1$ and plot for different charges q/M

should not be compared directly without checking the axis labels or Table 3. The flux curves in Fig. 1 also show that most of the model dependence is confined to the inner disk. For $r \sim 25M$, the plots converge, making the disk profiles indistinguishable in these regions; therefore, the ability to distinguish between models is effectively confined to the innermost radial range.

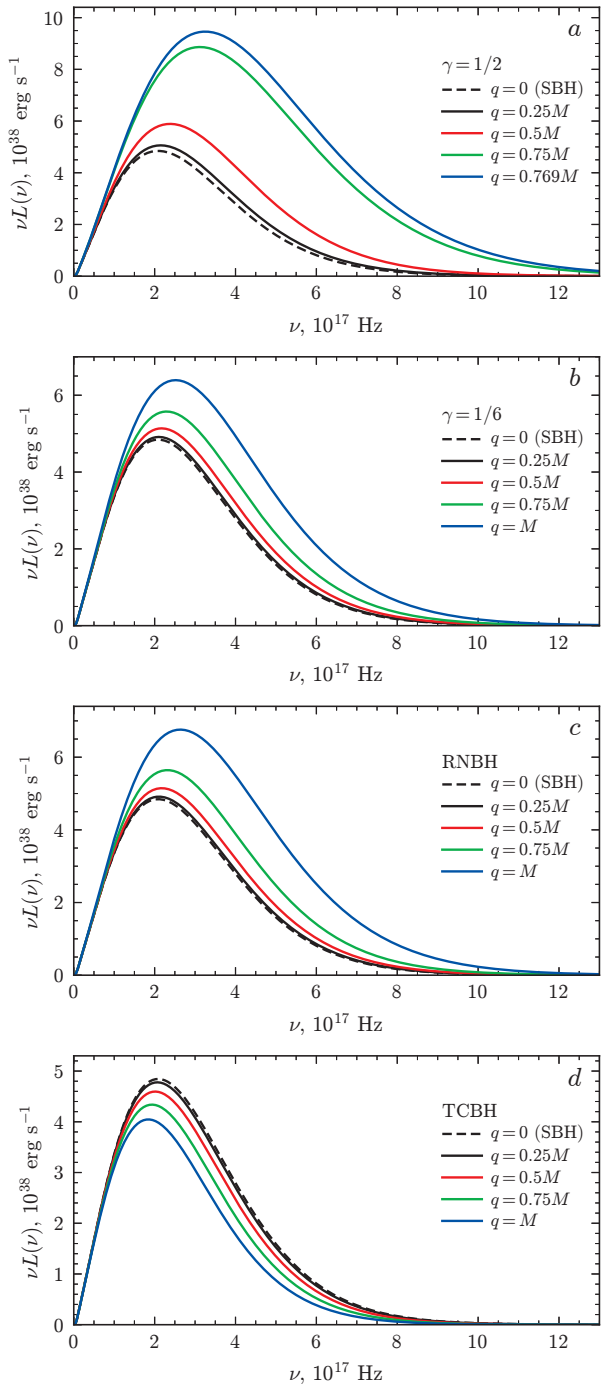


Fig. 3. Emission spectra $\nu L(\nu)$ vs frequency ν for thin accretion disks around the BVBH with $\gamma = 1/2$ (*a*), the BVBH with $\gamma = 1/6$ (*b*), the RNBH (*c*), and the TCBH (*d*). For both BVBH cases, we set $a = 1$ and plot for different charges q/M

Figure 2 shows the temperature profiles, and these follow the same ordering as the flux because of the Stefan–Boltzmann relation $F \propto T^4$. The key point here is that temperature responds more weakly than flux.

Table 4. Efficiency of the accretion disk around the BVBH for different values of γ and q compared with the RNBH and TCBH

BVBH			
$\gamma = 1/2$		$\gamma = 1/6$	
q/M	ε, %	q/M	ε, %
0	5.7191	0	5.7191
0.25	5.9786	0.25	5.8024
0.5	6.9812	0.5	6.0718
0.75	10.6445	0.75	6.6007
0.769	11.3949	1	7.5925
RNBH		TCBH	
q/M	ε, %	q/M	ε, %
0	5.7191	0	5.7191
0.25	5.8030	0.25	5.6392
0.5	6.0834	0.5	5.4207
0.75	6.6845	0.75	5.1121
1	8.1441	1	4.7635

For the $\gamma = 1/2$ case, the maximum flux increases by almost 9.4 times compared to the SBH, but the maximum temperature increases only from about $4.57{\cdot}10^6$ K to $7.99 \cdot 10^6$ K, which is slightly more than 1.75 times. This is a consequence of the fourth root dependence. Nevertheless, Fig. 2 reflects the same physical trend. The temperature profiles also show that the curves diverge strongly near the peak and then gradually merge at larger radii.

Figure 3 shows the observable spectra $\nu L(\nu)$. For the numerical calculations, we set the inclination $i = 0$ and the outer radius $r_\mathrm{f} = \infty$. Figures 3 *a*–*c* show that with increasing charge, the BVBH and RNBH disk brightness increases, and the peaks shift toward harder radiation. The opposite picture is observed for the TCBH in Fig. 3 *d*, where an increase in charge leads to a decrease in the disk luminosity. In the BVBH $\gamma = 1/2$ case, the peak of $\nu L(\nu)$ rises strongly and shifts to higher frequencies. This is the clearest radiative signature of that case. The $\gamma = 1/6$ case remains much closer to the RNBH: as the charge increases, its spectrum shifts toward higher frequencies, while the peak values remain slightly below those of the RNBH. Thus, we can conclude that the greatest differences between the considered black holes occur in the inner part of the disk, i. e., closer to the massive object. At large distances, i. e., as $r \to \infty$, the disk profiles become indistinguishable.

Table 4 demonstrates the efficiency of the accretion disk for the BVBH, RNBH, TCBH, and SBH. The efficiency increases from 5.72% for the SBH to 11.39% for the $\gamma = 1/2$ BVBH. For $\gamma = 1/6$, it increases more slightly, to 7.59%, and for the RNBH, to 8.14%. The TCBH model again shows the opposite trend, decreasing to 4.76%. This confirms that the inward motion of the inner disk edge generally correlates with increased efficiency, but it also shows that the detailed spacetime geometry matters. The comparison between the BVBH with $\gamma = 1/6$ and the RNBH shows that the efficiency of the RNBH is slightly higher than that of the BVBH. Thus, it can be said that the regularity of the black hole contributes to the disk profile, and depending on γ, it can slightly perturb the RNBH-like behavior.

It is important to emphasize that Figs. 1–3 and Tables 3 and 4 compare the models at the same numerical values of the original parameter q/M. For the BVBH, this does not correspond to the same asymptotic metric charge when γ is changed, because $Q_{\text{as}}^2 = 6\gamma q^2$. Moreover, as noted earlier, the largest value for $\gamma = 1/2$ lies almost at the extremal limit, whereas the largest value for $\gamma = 1/6$ is only 75% of its critical charge. Therefore, the larger flux, temperature, spectral luminosity, and efficiency obtained for the $\gamma = 1/2$ sequence in this section should be interpreted as the combined consequence of a larger normalized charge and greater proximity to extremality, rather than as an isolated dependence on γ. A controlled comparison at fixed normalized charge is presented in the next section.

5. EMISSIVITY PROPERTIES OF THE BALART – VAGENAS BLACK HOLE WITH NORMALIZED CHARGE

In the preceding sections, the radiative characteristics of the BVBH were compared for the same numerical values of the metric parameter q/M. However, for different values of γ, the parameter q does not correspond to the same asymptotic charge. Therefore, a direct comparison at fixed q/M may combine the influence of the nonlinear electrodynamic geometry with a difference in the effective charge measured in the asymptotic region.

For $a = 1$, the asymptotic expansion of the BVBH metric function at large distances is written as

$$f_{\text{BV}}(r) = 1 - \frac{2M}{r} + \frac{6\gamma q^2}{r^2} + O\left(r^{-3}\right). \tag{21}$$

Comparison with the Reissner – Nordström metric,

$$f_{\text{RN}}(r) = 1 - \frac{2M}{r} + \frac{Q^2}{r^2}, \tag{22}$$

naturally leads to the definition of the asymptotically normalized BVBH charge

$$Q_{\text{as}}^2 = 6\gamma q^2. \tag{23}$$

Thus, $Q_{\text{as}} = q$ for $\gamma = 1/6$, whereas $Q_{\text{as}} = \sqrt{3}\, q$ for $\gamma = 1/2$. In terms of Q_{as}, the exact BVBH metric function (9) can be rewritten as

$$f_{\text{BV}}(r) = 1 - \frac{2M}{r}\left(1 + \frac{Q_{\text{as}}^2}{6Mr}\right)^{-3}. \tag{24}$$

Since

$$\gamma q^2 = \frac{Q_{\text{as}}^2}{6}, \tag{25}$$

the parameter γ can be eliminated not only from the metric function but also from all quantities obtained solely from that metric. Substitution into Eqs. (13)–(15) therefore expresses Ω, $\widetilde{E}$, and $\widetilde{L}$ entirely in terms of M, r, and Q_{as}. The equation determining r_{ms} and the Page – Thorne flux integral inherit the same property. Hence, the equality of the two γ cases at fixed Q_{as} is an analytical identity. The coincident curves in Fig. 4 provide an independent numerical verification of this identity.

Although the leading charge-dependent term of the BVBH metric then agrees with that of the RNBH, the two geometries are not exactly identical. Expanding Eq. (24) to higher orders gives

$$f_{\text{BV}}(r) = 1 - \frac{2M}{r} + \frac{Q_{\text{as}}^2}{M^2}\left(\frac{M}{r}\right)^2 - \frac{Q_{\text{as}}^4}{3M^4}\left(\frac{M}{r}\right)^3 + \\ + \frac{5Q_{\text{as}}^6}{54M^6}\left(\frac{M}{r}\right)^4 + O\left(r^{-5}\right). \tag{26}$$

The terms beginning at order r^{-3} represent the nonlinear electrodynamic corrections that distinguish the regular BVBH geometry from the RNBH geometry at the same asymptotic charge. Therefore, comparison at fixed Q_{as}/M makes it possible to separate these higher order corrections from the effect of using different charge normalizations.

The normalization by Q_{as} also provides a common measure of proximity to the extremal BVBH configuration. Using the critical charge (11), one obtains

$$\frac{q}{q_c} = \frac{3Q_{\text{as}}}{4M}. \tag{27}$$

Equation (27) shows that a fixed value of Q_{as}/M is equivalent to a fixed value of q/q_c. Thus, for $a = 1$, normalizing by the asymptotic metric charge simultaneously removes the ambiguity caused by the different critical charges of the two γ sequences.

Table 5. Maximum disk observables for the BVBH at fixed q/q_c. The tabulated units are 10^{22} erg s^{-1} cm^{-2} for $F_{\max}$, 10^6 K for $T_{\max}$, and 10^{38} erg s^{-1} for $[\nu L(\nu)]_{\max}$

q/q_c	$Q_{\rm as}/M$	$F_{\max}$	$T_{\max}$	$[\nu L(\nu)]_{\max}$
0.00	0.0000	2.4644	4.5659	4.8444
0.25	0.3333	2.6742	4.6601	4.9694
0.50	0.6667	3.4939	4.9823	5.3991
0.75	1.0000	6.0665	5.7192	6.3927
1.00	1.3333	23.3940	8.0144	9.4889

Table 5 confirms the analytical degeneracy over the full range from weakly charged to extremal configurations. At every common value of q/q_c, the original parameters q/M differ between the two values of γ, but the normalized charge and all disk observables coincide. The equality of the independently calculated numerical values provides an internal consistency check. The final row should be understood as the extremal limiting configuration.

Figure 4 presents the time-averaged radiation flux, temperature distribution, and spectral luminosity for

$$\frac{Q_{\rm as}}{M} = 0.5. \tag{28}$$

For this normalized charge, the corresponding BVBH parameters are

$$\frac{q}{M} = 0.5 \quad \text{for} \quad \gamma = \frac{1}{6} \tag{29}$$

and

$$\frac{q}{M} = \frac{0.5}{\sqrt{3}} \simeq 0.2887 \quad \text{for} \quad \gamma = \frac{1}{2}. \tag{30}$$

Both cases have $q/q_c = 0.375$ and therefore represent the same relative distance from extremality. As follows directly from Eq. (24), the two BVBH curves in all three plots of Fig. 4 coincide within the numerical accuracy of the calculations. This result demonstrates that the differences between the $\gamma = 1/6$ and $\gamma = 1/2$ curves obtained at the same value of q/M originate from the different asymptotic charge normalization.

Figure 4 *a* shows that the normalized BVBH flux profile is very close to the RNBH profile. The maximum BVBH flux is

$$F_{\max}^{\rm BV} = 2.9763 \cdot 10^{22}\ \text{erg s}^{-1}\,\text{cm}^{-2}, \tag{31}$$

whereas for the RNBH at $Q/M = 0.5$,

$$F_{\max}^{\rm RN} = 2.9947 \cdot 10^{22}\ \text{erg s}^{-1}\,\text{cm}^{-2}. \tag{32}$$

The BVBH maximum is therefore approximately 0.61% lower than the RNBH maximum. The enlarged

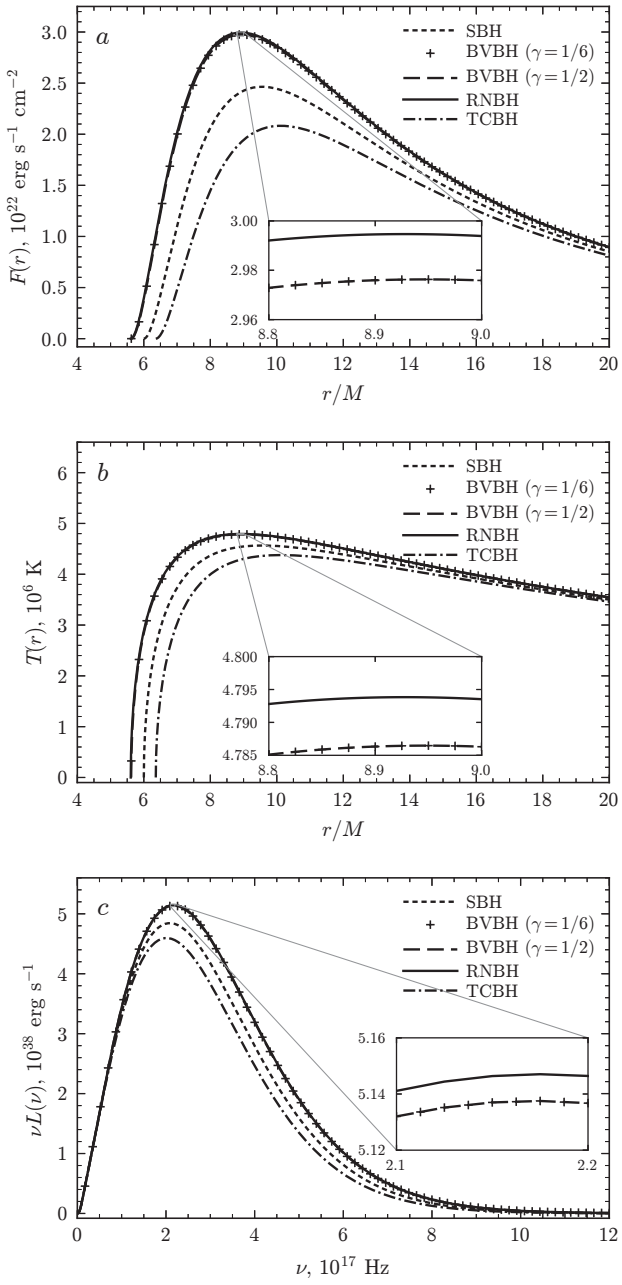


Fig. 4. Comparison of the time-averaged radiation flux $F(r)$ (*a*), the temperature distribution $T(r)$ (*b*), and the spectral luminosity $\nu L(\nu)$ (*c*) for thin accretion disks around the BVBH, RNBH, SBH, and TCBH. For the BVBH, $a = 1$ and $Q_{\rm as}/M = 0.5$, corresponding to $q/M = 0.5$ for $\gamma = 1/6$ and $q/M = 0.5/\sqrt{3} \simeq 0.2887$ for $\gamma = 1/2$. The RNBH and TCBH comparison curves are calculated for the charge parameter $q/M = 0.5$, while the SBH corresponds to $q = 0$. The insets magnify the regions near the maxima. At fixed $Q_{\rm as}/M$, the two BVBH curves coincide within numerical accuracy and lie slightly below the RNBH curve

region in Fig. 4 *a* is required to distinguish the two profiles near their maxima. The slight decrease in the BVBH flux is consistent with its marginally stable radius, $r_{\rm ms} = 5.6191M$, being slightly larger than the corresponding RNBH value, $r_{\rm ms} = 5.6066M$.

The temperature distributions in Fig. 4 *b* exhibit the same ordering as the flux profiles. The maximum temperatures are

$$T_{\max}^{\rm BV} = 4.7868 \cdot 10^6 \text{ K} \tag{33}$$

and

$$T_{\max}^{\rm RN} = 4.7939 \cdot 10^6 \text{ K}. \tag{34}$$

The BVBH temperature maximum is only approximately 0.15% lower than the RNBH value. The smaller relative difference in temperature follows from the Stefan – Boltzmann relation $T \propto F^{1/4}$, according to which changes in the radiation flux produce weaker relative changes in the disk temperature.

A similar result is obtained for the spectral luminosity shown in Fig. 4 *c*. For the normalized BVBH metric,

$$[\nu L(\nu)]_{\max}^{\rm BV} = 5.1375 \cdot 10^{38} \text{ erg} \cdot \text{s}^{-1}, \tag{35}$$

while the corresponding RNBH value is

$$[\nu L(\nu)]_{\max}^{\rm RN} = 5.1471 \cdot 10^{38} \text{ erg} \cdot \text{s}^{-1}. \tag{36}$$

The difference between the spectral maxima is approximately 0.19%. The peaks and the overall spectral shapes are also nearly identical, and the small separation between the BVBH and RNBH spectra can be clearly seen only in the enlarged region near the maximum.

The same small difference is found in the kinematic quantities and in the accretion efficiency. At $Q_{\rm as}/M = 0.5$, the BVBH has

$$r_{\rm ms}^{\rm BV} = 5.6191M, \qquad \varepsilon^{\rm BV} = 6.0718\%, \tag{37}$$

whereas the corresponding RNBH values are

$$r_{\rm ms}^{\rm RN} = 5.6066M, \qquad \varepsilon^{\rm RN} = 6.0834\%. \tag{38}$$

Thus, relative to the RNBH, the BVBH marginally stable radius is approximately 0.22% larger and its efficiency is approximately 0.19% lower. Together with the differences in $F_{\max}$, $T_{\max}$, and $[\nu L(\nu)]_{\max}$, these values demonstrate quantitatively that the higher order nonlinear electrodynamic correction is small and suppressive at this normalized charge.

For comparison, the BVBH and RNBH profiles in Fig. 4 lie above the Schwarzschild profiles, whereas the TCBH produces lower flux, temperature, and spectral luminosity. At larger radial distances, the flux and temperature curves gradually approach one another because the higher order corrections to the metric become negligible. Similarly, the differences between the spectral profiles are concentrated mainly near the maximum.

The normalized charge analysis therefore changes the interpretation of the results obtained at fixed q/M. At fixed $Q_{\rm as}/M$, the cases $\gamma = 1/6$ and $\gamma = 1/2$ do not produce different metric-based accretion disk observables for $a = 1$. The residual difference between the BVBH and RNBH profiles is caused exclusively by the higher order nonlinear electrodynamic terms in Eq. (24). For $Q_{\rm as}/M = 0.5$, these corrections are small and lead to a slight decrease in the flux, temperature, and spectral luminosity relative to the RNBH case.

This degeneracy applies to the neutral particle Novikov – Thorne model considered here, in which the disk observables are determined solely by the spacetime geometry. It does not necessarily imply that all electromagnetic properties of the underlying nonlinear electrodynamic solutions are identical, because quantities directly coupled to the electromagnetic field may retain an explicit dependence on γ.

6. CONCLUSION

Studying black holes supported by nonlinear electrodynamics is important because such solutions offer one of the most compelling ways to address the singularity problem of classical charged black holes while remaining close to general relativity in the weak field regime. In the regular solutions developed by Ayón-Beato and García [36] and later extended by Balart and Vagenas [1], the electromagnetic source becomes nonlinear only where the field is strongest, yet the theory still approaches Maxwell electrodynamics in the weak field limit. This makes nonlinear electrodynamics black holes physically meaningful extensions of the standard charged black hole picture rather than purely phenomenological deformations.

In this setting, comparison with the RNBH is especially informative, but it requires a common charge normalization. At the same numerical value of the original parameter q/M, the $\gamma = 1/2$ BVBH sequence has a larger asymptotic metric charge than the $\gamma = 1/6$ sequence and also reaches configurations much closer to extremality. The substantial increase in the disk

flux, temperature, spectral luminosity, and efficiency observed in that parameterization therefore cannot be attributed uniquely to an independent effect of γ.

Introducing $Q_{\rm as}^2 = 6\gamma q^2$ resolves this ambiguity. For $a = 1$, the exact BVBH metric depends on γ and q only through $Q_{\rm as}$. Consequently, the $\gamma = 1/6$ and $\gamma = 1/2$ cases are exactly degenerate regarding the Novikov – Thorne observables at fixed $Q_{\rm as}/M$. Within the model studied here, thin-disk observations can therefore constrain the normalized charge and the resulting spacetime geometry, but cannot constrain γ independently.

The controlled comparison with the RNBH isolates the higher order nonlinear electrodynamic terms beginning at order r^{-3}. At $Q_{\rm as}/M = 0.5$, these terms shift the marginally stable orbit slightly outward and reduce the flux, temperature, spectral luminosity, and efficiency by less than one percent relative to the RNBH. Thus, for this normalized charge, the BVBH closely mimics the RNBH, while the remaining nonlinear electrodynamic signature is small and suppressive rather than enhancing.

More broadly, recent thin disk analyses of regular black holes sourced by nonlinear electrodynamics reach the same qualitative finding: depending on the model parameters, these spacetimes may either closely mimic classical charged black holes or depart from them significantly in the marginally stable orbit location, emitted spectrum, and efficiency [8–11]. For that reason, BVBHs are important both theoretically, as nonsingular charged black hole solutions, and observationally, as test spacetimes whose deviations may be constrained by luminosity spectra and future imaging or ray-tracing studies.

Funding. The study was not sponsored.

Conflict of interest. The authors declare that they have no conflicts of interest.

Authors' contributions. The contributions of the authors are equal.

REFERENCES

1. L. Balart and E. C. Vagenas, Phys. Rev. D **90**, 124045 (2014).

2. P. T. Kondratko, L. J. Greenhill, and J. M. Moran, Astrophys. J. **678**, 87 (2008).

3. C. M. Urry and P. Padovani, Publ. Astron. Soc. Pac. **107**, 803 (1995).

4. N. I. Shakura and R. A. Sunyaev, Astron. Astrophys. **24**, 337 (1973).

5. I. D. Novikov and K. S. Thorne, in *Black Holes*, ed. by C. DeWitt and B. DeWitt, Gordon and Breach, New York (1973), p. 343.

6. K. S. Thorne, Astrophys. J. **191**, 507 (1974).

7. D. N. Page and K. S. Thorne, Astrophys. J. **191**, 499 (1974).

8. M. Khoshrangbaf, K. Atazadeh, H. Motavalli et al., New Astron. **117**, 102354 (2025).

9. Y. Kurmanov, K. Boshkayev, T. Konysbayev et al., Phys. Dark Universe **46**, 101566 (2024).

10. P. I. Dyadina and N. A. Avdeev, Space, Time Fundam. Interact., No. 3–4, 63 (2023).

11. R. Kh. Karimov, R. N. Izmailov, A. Bhattacharya et al., Eur. Phys. J. C **78**, 788 (2018).

12. R. Kh. Karimov, R. N. Izmailov, A. A. Potapov et al., Eur. Phys. J. C **82**, 239 (2022).

13. I. Banerjee, S. Chakraborty, and S. SenGupta, Phys. Rev. D **96**, 084035 (2017).

14. I. Banerjee, S. Chakraborty, and S. SenGupta, Phys. Rev. D **100**, 044045 (2019).

15. P. Dyadina and N. Avdeev, Eur. Phys. J. C **84**, 103 (2024).

16. P. I. Dyadina and N. A. Avdeev, Class. Quantum Grav. **43**, 085001 (2026).

17. T. Harko, Z. Kovács, and F. S. N. Lobo, Class. Quantum Grav. **28**, 165001 (2011).

18. T. Harko, Z. Kovács, and F. S. N. Lobo, Class. Quantum Grav. **27**, 105010 (2010).

19. D. Pérez, G. E. Romero, and S. E. Perez Bergliaffa, Astron. Astrophys. **551**, A4 (2013).

20. C. S. J. Pun, Z. Kovács, and T. Harko, Phys. Rev. D **78**, 024043 (2008).

21. M. Heydari-Fard and H. R. Sepangi, Phys. Lett. B **816**, 136276 (2021).

22. S. L. Shapiro, Phys. Rev. D **95**, 101303 (2017).

23. H. Reissner, Ann. Phys. (Berlin) **355**, 106 (1916).

24. N. Dadhich, R. Maartens, P. Papadopoulos et al., Phys. Lett. B **487**, 1 (2000).

25. T. Manna, F. Rahaman, S. Molla et al., Gen. Relativ. Gravit. **50**, 54 (2018).

26. I. Radinschi, T. Grammenos, F. Rahaman et al., Universe **6**, 169 (2020).

27. H. Zhang, N. Zhou, W. Liu et al., Gen. Relativ. Gravit. **54**, 110 (2022).

28. M. Sharif and S. Sadiq, JETP **126**, 194 (2018) [M. Sharif and S. Sadiq, ЖЭТФ **153**, 232 (2018)].

29. C. Dagum, Écon. Appl. **30**, 413 (1977).

30. R. Casadio, A. Fabbri, and L. Mazzacurati, Phys. Rev. D **65**, 084040 (2002).

31. K. K. Nandi, R. N. Izmailov, R. Kh. Karimov et al., Ann. Phys. **470**, 169802 (2024).

32. S. O. Alexeyev, B. N. Latosh, V. A. Prokopov et al., JETP **128**, 720 (2019) [С. О. Алексеев, Б. Н. Латош, В. А. Прокопов и др., ЖЭТФ **155**, 847 (2019)].

33. T. Harko, Z. Kovács, and F. S. N. Lobo, Phys. Rev. D **78**, 084005 (2008).

34. T. Harko, Z. Kovács, and F. S. N. Lobo, Phys. Rev. D **79**, 064001 (2009).

35. D. F. Torres, Nucl. Phys. B **626**, 377 (2002).

36. E. Ayón-Beato and A. García, Phys. Rev. Lett. **80**, 5056 (1998).